Driving skyrmions in flow regime in synthetic ferrimagnets

Sougata Mallick[1,*], Yanis Sassi[1], Nicholas Figueiredo Prestes[1], Sachin Krishnia[1], Fernando Gallego[1], Luis M. Vicente Arche[1], Thibaud Denneulin[2], Sophie Collin[1], Karim Bouzehouane[1], André Thiaville[3], Rafal E. Dunin-Borkowski[2], Vincent Jeudy[3], Albert Fert[1], Nicolas Reyren[1] and Vincent Cros[1]

[1] Laboratoire Albert Fert, CNRS, Thales, Université Paris-Saclay, 91767 Palaiseau, France

[2]Forschungszentrum Jülich, ER-C for Microscopy and Spectroscopy with Electrons, Jülich, Germany

[3]Laboratoire de Physique des Solides, CNRS, Université Paris-Saclay, 91400 Orsay, France

** Present Affiliation: Department of Physics and Nanotechnology, College of Engineering and Technology, SRM Institute of Science and Technology, Kattankulathur, 603203, Tamil Nadu, India*

Supplementary Information

Role of capping layer in protecting oxidation of Tb:

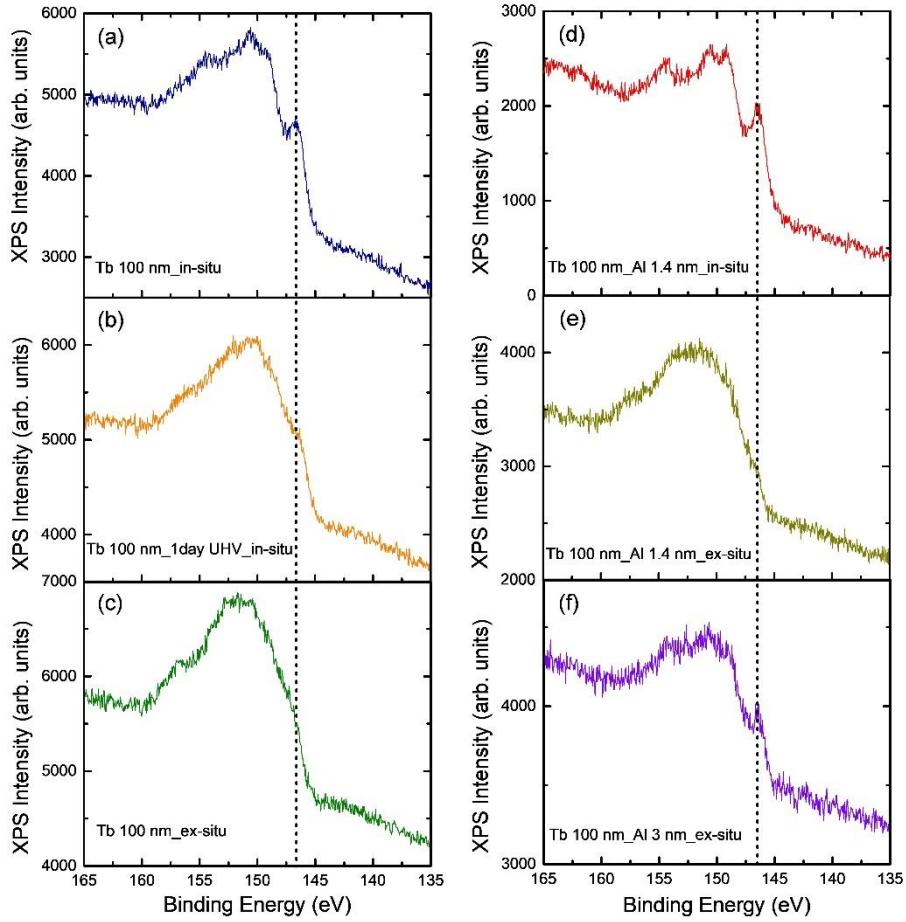

Fig. S1: XPS measurements to check oxidation of Tb. XPS measurements of the following: (a) Tb 100 nm (no capping layer) measured in-situ after deposition, (b) Tb 100 nm (no capping layer) measured in-situ after 1 day in UHV after deposition, (c) Tb 100 nm (no capping layer) measured ex-situ, (d) Tb 100 nm (Al 1.4nm capping layer) measured in-situ, (e) Tb 100 nm (Al 1.4nm capping layer) measured ex-situ, (f) Tb 100 nm (Al 3nm capping layer) measured ex-situ. The dotted line at ~147 eV corresponds to peak associated to metallic Tb 4*d*.

As Tb is recognized as an active element prone to oxidation, we deposit a protective 5 nm thick capping layer (comprising 3 nm of Al and 2 nm of Pt) across all samples addressed in the manuscript, in order to safeguard Tb from oxidation and preserve its metallic properties. To validate the efficacy of this protective measure, XPS measurements have been conducted on both single layer uncapped Tb films

of 100 nm thickness and Tb films of the same thickness capped with an Al layer alone. In our XPS analyses, we deliberately employed a thicker Tb layer to ensure robust signal strength. Nevertheless, we also explored Tb thicknesses as low as 1 nm, yielding qualitatively similar results albeit with diminished intensity. It is important to note that XPS primarily probes the surface layers of a material, typically only a few nm deep. Consequently, the samples discussed in our paper hindered direct examination of the Tb layer due to the presence of the 5nm thick metallic capping layers.

In Fig. S1 (a)–(f) we show the in-situ and ex-situ XPS measurements for uncapped Tb 100 nm and Tb 100 nm films capped with Al layer with various thicknesses, respectively. For reference, we have marked a dotted black line at 147 eV which corresponds to the metallic peak associated to Tb 4*d*. In Fig. S1 (a) (blue spectra), we observe the distinctive sharp peak of metallic Tb 4*d* at 147 eV for Tb 100 nm thin film (uncapped), measured in-situ in UHV immediately after the growth in the sputtering chamber. Additionally, a minor proportion of O 1*s* is detected. Notably, the Tb 4*d* peak flattens upon storing the sample in UHV for a day (yellow spectra in Fig. S1 (b)), indicating propensity of Tb for oxidation even under UHV conditions. Subsequent exposure to ambient atmosphere results in complete oxidation of Tb, eliminating any presence of metallic Tb (green spectra in Fig. S1 (c)). Subsequently, we examined a separate sample with the same Tb thickness, this time capped with 1.4 nm of Al in-situ in UHV (red spectra in Fig. S1 (d)). Interestingly, the metallic Tb peak is heightened compared to the uncapped Tb sample. This suggests that the 1.4 nm Al capping layer results into a partial protection against Tb oxidation during and immediately after deposition, as confirmed by the negligible Tb oxidation within the UHV chamber during this process. However, XPS measurement on the same sample after exposure to ambient conditions demonstrates Tb oxidation once again (dark yellow spectra in Fig. S1 (e)), indicating that although the 1.4 nm Al layer shields Tb within the UHV chamber, it fails to do so in ambient conditions. Finally, we examine another sample, this time with the Tb layer capped with a thick 3 nm Al, post-exposure to ambient conditions using XPS (violet spectra in Fig. S1 (f)). In this case, we observe metallic Tb peaks corresponding to Tb 4*d*. Consequently, we deduce that while Tb exhibits a tendency for oxidation, this can be largely minimized by capping it with 3 nm Al. Importantly, we note that the samples discussed in the paper also feature an additional 2 nm Pt capping layer to safeguard the top Al layer from oxidation in ambient conditions. Additionally, we have obtained signature of metallic Tb in XMCD experiments performed on the multilayer samples discussed in the manuscript.

M-H loops for the samples:

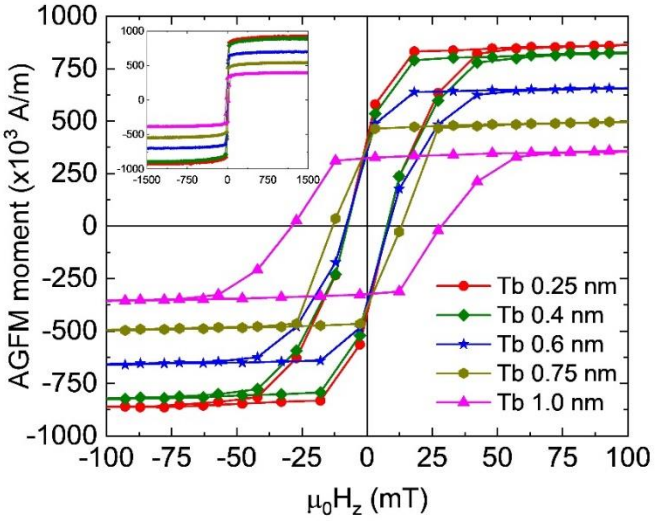

Fig. S2: Hysteresis loops measured using AGFM in perpendicular mode for all the multilayer samples with various Tb thicknesses.

In Fig. S2, we present the hysteresis loops for all the samples measured using AGFM in perpendicular geometry. It can be seen that the magnetization of the samples decreases continuously with increasing Tb thickness confirming the increase of antiferromagnetic coupling (relative increase of Tb moment opposite to Co ones) between Co and Tb. The thickness of Co (1.3 nm) in the multilayers has been

chosen in such a way that the effective anisotropy of the multilayers is small enough and hence facilitates skyrmion stabilization. However, it can be seen from the hysteresis loops that the anisotropy of the systems starts increasing (near 100% remanence) after $t_{Tb} > 0.6$ nm. The consequence of such increase in anisotropy can be also observed during the current induced dynamics measurements in which beyond $t_{Tb} > 0.6$ nm, we have succeeded to stabilize only chiral DWs in the system instead of skyrmions. The magnetization and anisotropy behaviour of the samples are discussed in Fig. 2 of the main manuscript.

Estimation of DMI:

In order to estimate the interfacial DMI in the heterostructure, BLS measurements have been performed in Damon-Eschbach geometry on the single-layer samples Si/SiO_2//Ta (5 nm)/Pt (8 nm)/Co (1 nm)/Tb (0.25, 0.5, and 1.0 nm)/Al (3 nm)/Pt (2 nm). In ultrathin films, the spin-wave frequency is expected to be:

$$f = f_0 \pm f_{\mathrm{DMI}} \equiv f_0 \pm \frac{\gamma}{\pi M_s} D_{\mathrm{eff}} k_{\mathrm{sw}}$$

where, γ is the gyromagnetic ratio $\frac{\gamma}{2\pi} = g \times 13.996$ GHz/T, with $g = 2.14 \pm 0.27$, k_{sw} is the spin-wave wavevector, M_s is the spontaneous magnetization, and effective DMI $D_{\mathrm{eff}} = \frac{D_s}{t}$ with D_s being the interfacial DMI energy, and t is the thickness of the magnetic material, here Co and Tb, $t = t_{\mathrm{Co}} + t_{\mathrm{Tb}}$. The DMI can be calculated using $\Delta f = f_S(-k) - f_{AS}(k) = \frac{2\gamma}{\pi M_S} D_{eff} k_{sw}$. Fig. S3(a) represents typical BLS spectra for the sample as a function of different external magnetic fields. The difference of frequency peaks between the Stokes and anti-Stokes lines as a function of the wave-vector is plotted in Fig. S3(b). We calculate the slope of Δf by considering both the center frequency as well as the maximum frequency, and estimate the difference in the error bar. Using the aforementioned equation, we estimate the value of interfacial DMI $D_s = -1.62 \pm 0.20$ pJ/m for $t_{\mathrm{Tb}} = 0.25$ nm. The anisotropy field (H_K) of the samples increases significantly with the Tb thickness increase ($\mu_0 H_K \sim$ 1.0 T, 1.4 T, >2.2 T for the samples with $t_{Tb} = 0.25, 0.5,$ and 1.0 nm, respectively) confirming the increase of AFM coupling with Tb. The large iDMI combined with the dipolar coupling between the multilayers facilitates the stabilization of skyrmions in the samples even with such large anisotropy. Extraction of the iDMI for the samples with larger Tb thickness was not possible due to the experimental limit of the highest possible applicable external magnetic field.

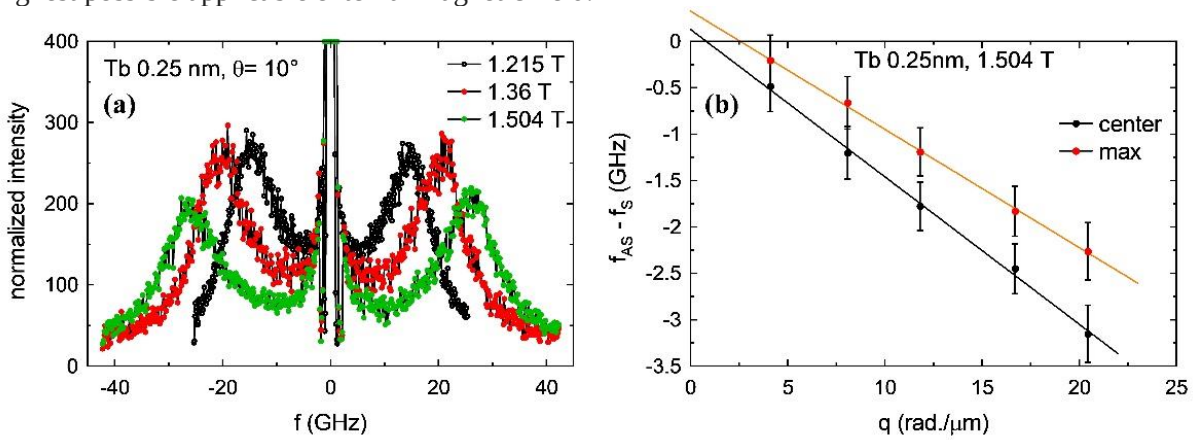

Fig. S3: Estimation of DMI using BLS measurements. (a) BLS spectra for the single layer sample with $t_{\mathrm{Tb}} = 0.25$ nm as a function of various applied magnetic fields. (b) Plot of the frequency difference between the Stokes and anti-Stokes peaks as a function of the spin wave vector.

Optimization of the magnetic force microscopy tips:

Previous reports involving MFM imaging of skyrmions demonstrate that skyrmions can be significantly distorted, nucleated, annihilated, as well as driven locally by the stray field of the magnetic tip predominantly during the topography scan [1–5]. Hence, it is crucial to minimize the tip-induced perturbation of textures for accurate estimation of skyrmion velocity. Therefore, we have used 5 nm

(minimum to detect signal) thick homemade $Co_{40}Fe_{40}B_{20}$ tips with low stray field. Also, a capping layer of Al has been added with thickness ranging between 30 – 50 nm depending on the sample specificity. This Al capping ensures a minimal distance between the tip and the magnetic thin film during the topographical image, during which the tip-sample interaction is maximum. Additionally, we reduce the influence of magnetic tip on the position of the skyrmions along the track (y-axis) by using the fast scan axis (direction where the tip induced distortion is maximum) along the transverse direction of the track (x-axis). This ensures that even in presence of any remaining perturbation, the textures would be mostly modified along the transverse direction and not towards the direction of the skyrmion motion.

Magnetization of the Pt/Co/Tb multilayers:

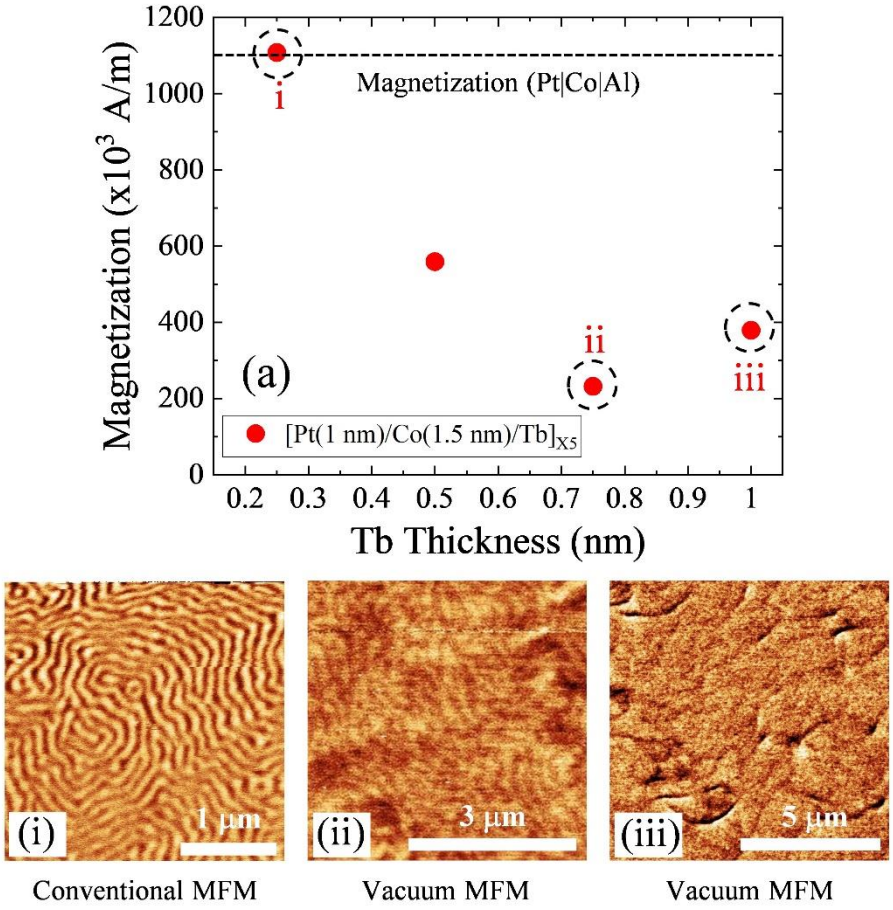

Fig. S4: (a) Room temperature saturation magnetization measured by MFM in [Pt (1 nm)/Co (1.5 nm)/Tb (t_{Tb})]$_{\times 5}$ multilayers vs. Tb thickness. The black dotted line represents the magnetization measured in Pt|Co|Al. (i) – (iii) Phase signals at demagnetized state measured using conventional MFM (i: $t_{\mathrm{Tb}} = 0.25$ nm), and vacuum MFM (ii: $t_{\mathrm{Tb}} = 0.75$ nm, iii: $t_{\mathrm{Tb}} = 1.0$ nm) on the samples marked in (a). The scale bar for all the images performed using conventional and vacuum MFM are 0.5° and 1°, respectively.

The evolution of the total magnetization (calculated for combined thickness of Co and Tb layers) as a function of Tb thickness in [Pt (1 nm)/Co (1.5 nm)/Tb (t_{Tb})]$_{\times 5}$ multilayers is plotted in Fig. S4(a) together with the magnetization for Pt|Co|Al multilayers [6] displayed by the black dotted line. We find that the magnetization decreases monotonically with the increase of Tb thickness from about one monolayer (~ 0.3 nm) up to about 3 ML (1 nm). In Fig. S4: (i), we show the phase signal at demagnetized state measured using conventional MFM on the sample with $t_{\mathrm{Tb}} = 0.25$ nm. For thicker Tb ($t_{\mathrm{Tb}} > 0.5$ nm), due to significant reduction in the magnetization (and thereby in the stray field), magnetic imaging using conventional MFM is no longer possible. Hence, for samples with $t_{\mathrm{Tb}} = 0.75$ nm, and 1 nm, respectively, we have used a vacuum MFM to image their magnetic configuration. For $t_{\mathrm{Tb}} = 0.75$ nm, we obtain a labyrinth state albeit with the phase signal that is only about 10% of the sample with $t_{\mathrm{Tb}} = 0.25$ nm (see Fig. 2 (ii)). For $t_{\mathrm{Tb}} = 1.0$ nm, the magnetization lies in-plane showing

typical domain configuration as shown in Fig. 2 (iii)). The rather low Pt thickness (1 nm) is the possible reason that with enhanced Tb thickness the heterostructure transit from out-of-plane to in-plane effective anisotropy. Additionally, putting current through the patterned tracks in these samples led to parasitic skyrmion nucleation. Hence, subsequently, the thickness of the Pt layer is increased from 1 to 3 nm in the torque optimized samples to enhance the PMA as well as the torque efficiency of the samples.

Skyrmion Hall effect:

In Fig. S5: (a) – (c), we describe the motion of skyrmions in //Ta(5 nm)/Pt(5 nm)/[Pt (3 nm)/Co (1.3 nm)/Tb (0.6 nm)/Al (3 nm)]$_{\times 5}$ multilayers after application of two successive 10 ns wide current pulses with $J = 3.27 \times 10^{11}$ A/m^2 in a 3 µm wide track. Contrary to the results obtained in 1µm wide track shown in Fig. 4 (a) – (d), in the 3 µm wide tracks, a sizeable deflection of the skyrmions transverse to the direction of the applied current due to the skyrmion Hall effect is observed. The measured value of skyrmion Hall angle is ~ 29° and does not vary significantly with J. However, it should be noted that, due to small size of the skyrmions, the experiments performed in the 3 µm wide tracks were limited in J ($2.8 \times 10^{11} - 3.8 \times 10^{11}$ A/m^2) since higher current densities led to nucleation of new skyrmions which made the tracking of individual skyrmions non-feasible. We have further estimated the skyrmion Hall angle ($\theta_{SHA} = \arctan\left(\frac{1}{\alpha}\frac{2\Delta}{R}\right)$) by using experimentally obtained values of different micromagnetic parameters: $\alpha, \Delta,$ and R. The red, and blue, dotted lines are the predicted skyrmion Hall angles for the samples with $t_{\mathrm{Tb}} = 0.25$, and 0.5 nm, respectively. We observe that the experimentally obtained value of ~ 29° is in good agreement with the predicted value of 27.5°. The additional reduction of the skyrmion Hall angle arises from the edge repulsion of the tracks. The movie of skyrmion motion in a 3 µm wide track is shown as supplementary video file. To complete this analysis, we have also calculated and experimentally measured the skyrmion Hall angle in a multilayer with no Tb layer i.e. a ferromagnetic multilayer of Pt|Co|Al with same thicknesses of the individual layers. Using experimentally determined α, Δ, R parameters, the predicted skyrmion Hall angle in this sample is 56.6° while the one determined experimentally is about 45° measured in a 5 µm wide track. This confirms that the skyrmion Hall angle in ferrimagnetic multilayers diminishes in the presence of Tb, as a result of the partial counterbalance of angular momentum between the Co and Tb layers. In Fig. S5(d), we present the comparison of skyrmion Hall angle of our sample with selected reports from the literature. This observation further solidifies the evidence indicating a reduction in the skyrmion Hall angle within our sample. This decrease in the skyrmion Hall angle, coupled with the presence of finite edge repulsion, collectively facilitates the straight-line motion of the skyrmions as detailed in the manuscript.

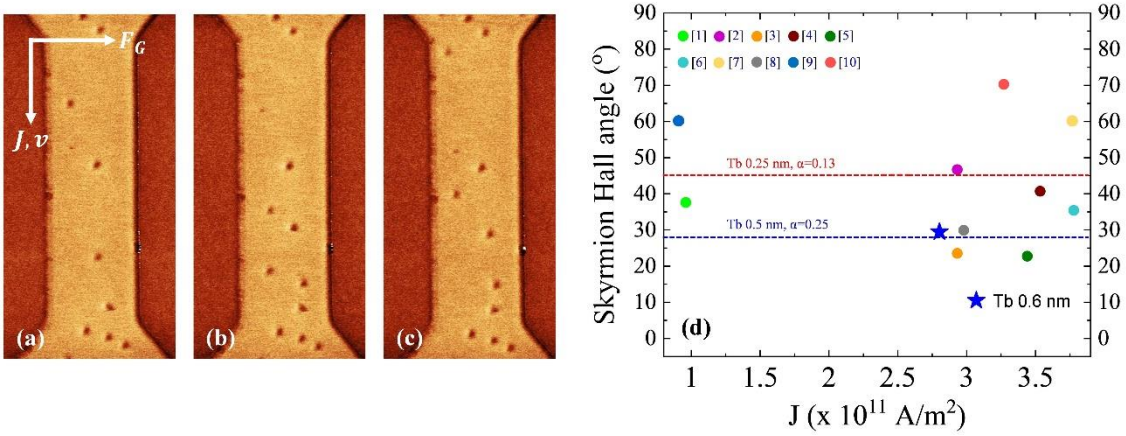

Fig. S5: Estimation of skyrmion Hall angle. (a) – (c) motion of skyrmions in [Pt (3 nm)/Co (1.3 nm)/Tb (0.6 nm)/Al (3 nm)]$_{\times 5}$ multilayers after application of two successive 10 ns wide current pulses with $J = 3.27 \times 10^{11}$ A/m^2 in a 3 µm wide track. (d) Comparison of skyrmion Hall effect of the sample: $t_{\mathrm{Tb}} = 0.6$ nm (blue star), with the existing literature. The red, and blue dotted lines are the predicted skyrmion Hall angles for the samples with $t_{\mathrm{Tb}} = 0.25$, and 0.5 nm, respectively. The numbered data points [1-10] in the figure are taken from refs. [7], [8], [9], [10], [11], [12], [13], [14], [15], [16], respectively.

Current induced dynamics of various magnetic textures:

The current induced dynamics in the tracks made from multilayers with $t_{\mathrm{Tb}} = 0.6$, 0.75, and 1.0 nm are displayed in Fig. S6. The typical magnetic states after nucleation by a current pulse at finite external magnetic field is shown in Fig. S6(a) – (c). It can be seen that unlike the $t_{\mathrm{Tb}} = 0.6$ nm sample, the skyrmionic state cannot been obtained in the other two samples. This is corroborated to the significant increase in the anisotropy in the samples with $t_{\mathrm{Tb}} = 0.75$, and 1.0 nm (also can be seen in Fig. 2(ii), (iii)). The value of anisotropy field in the single layer Co(1 nm)/Tb(1 nm) sample is larger than 2.2 T, which is too large to allow the formation of a skyrmionic phase, even in the presence of large iDMI in the system. Nevertheless, the magnetic domains in the $t_{\mathrm{Tb}} = 0.75$ nm and 1 nm samples can be also moved through spin-orbit torques using current pulses followed by similar protocol employed to drive the skyrmions in the lower Tb thickness samples. Velocity of the magnetic domains/textures as a function of the applied current density for the samples with $t_{\mathrm{Tb}} = 0.6$, 0.75, and 1.0 nm is shown in Fig. S6(d). It can be observed that the response of the domains in the thicker Tb samples is similar to that of the skyrmions in the sample with $t_{\mathrm{Tb}} = 0.6$ nm. This indicates that the optimum range to obtain high skyrmion mobility in this system is to work with the multilayer sample with $t_{\mathrm{Tb}} = 0.6$ nm.

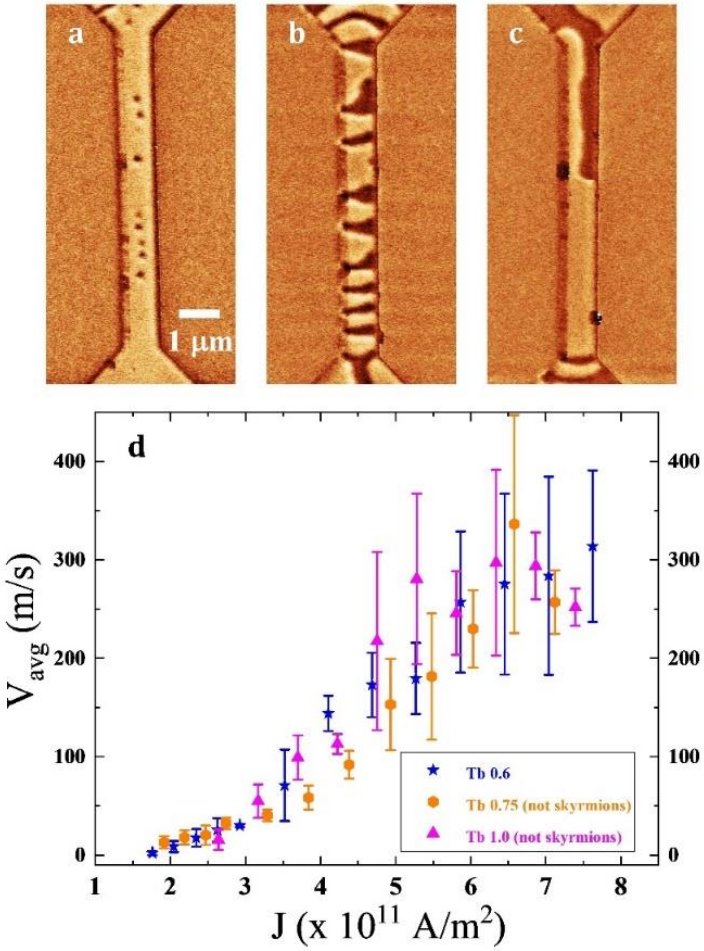

Fig. S6: Current induced motion of magnetic textures. Different types of magnetic textures stabilized in the nanotracks under the influence of an external perpendicular field and a nucleating current pulse for the multilayer samples with (a) $t_{Tb} = 0.6$ nm, (b) $t_{Tb} = 0.75$ nm, and (c) $t_{Tb} = 1.0$ nm, respectively. (d) Comparison of average skyrmion velocity *vs.* current density for the three aforementioned samples. Error bars corresponding to each data points represent the standard deviation of the velocity.

Estimation of gyromagnetic ratio:

The frequency (f_{res}) of a spin wave in a magnetic material in the presence of an external magnetic field (H) can be described by the following dispersion relation:

$$f_{\mathrm{res}} = \frac{\gamma}{2\pi}\sqrt{H(H + H_{ani} + Ak^2)}$$

where, $\gamma = \frac{g\mu_B}{\hbar}$ is the gyromagnetic ratio (g: Landé g factor), H_{ani} is the anisotropy field, and A is exchange stiffness constant. For uniform mode ($k = 0$), the spin wave frequency simplifies to $f_{\mathrm{res}} = \frac{g\mu_B}{h}H$. From BLS measurement, f_{res} has been plotted as a function of H for the single layer samples with $t_{\mathrm{Tb}} = 0.25$ nm (Fig. S7(a)) and $t_{\mathrm{Tb}} = 0.5$ nm (Fig. S7(b)). From the slope of the curves, we obtain $g = 2.14 \pm 0.07$ and 2.32 ± 0.01 for $t_{\mathrm{Tb}} = 0.25$ and 0.5 nm, respectively. This confirms that increasing the Tb thickness leads to the enhancement of the Gyromagnetic ratio γ.

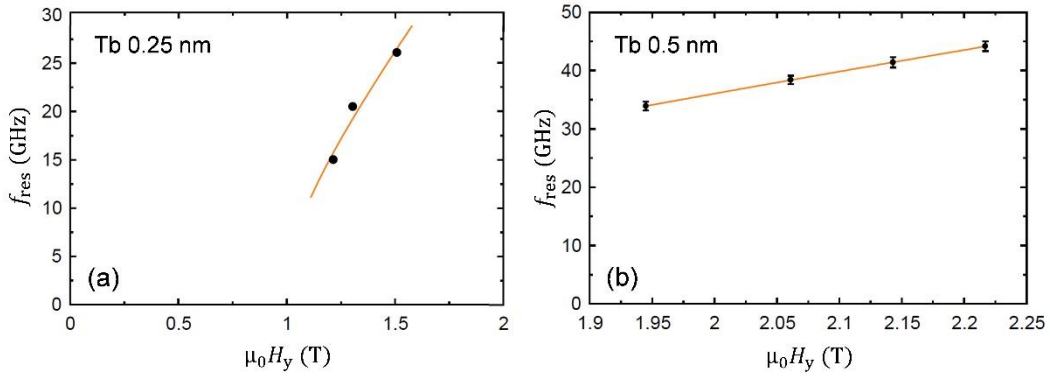

Fig. S7: Estimation of Gyromagnetic ratio using BLS measurements. Resonance frequency (f_{res}) as a function of in-plane external magnetic field (H_y) for (a) $t_{\mathrm{Tb}} = 0.25$ nm and (b) $t_{\mathrm{Tb}} = 0.5$ nm.

References:

[1] M. Zelent et al., *Skyrmion Formation in Nanodisks Using Magnetic Force Microscopy Tip*, Nanomaterials **11**, (2021).

[2] A. Casiraghi, H. Corte-León, M. Vafaee, F. Garcia-Sanchez, G. Durin, M. Pasquale, G. Jakob, M. Kläui, and O. Kazakova, *Individual Skyrmion Manipulation by Local Magnetic Field Gradients*, Commun Phys **2**, 145 (2019).

[3] Z. Qin, C. Jin, H. Xie, X. Li, Y. Wang, J. Cao, and Q. Liu, *Size-Tunable Skyrmion Bubbles in Ta/CoFeB/MgO Multilayers*, J Phys D Appl Phys **51**, 425001 (2018).

[4] S. Zhang et al., *Direct Writing of Room Temperature and Zero Field Skyrmion Lattices by a Scanning Local Magnetic Field*, Appl Phys Lett **112**, 132405 (2018).

[5] A. v Ognev et al., *Magnetic Direct-Write Skyrmion Nanolithography*, ACS Nano **14**, 14960 (2020).

[6] F. Ajejas, Y. Sassi, W. Legrand, S. Collin, J. Peña Garcia, A. Thiaville, S. Pizzini, N. Reyren, V. Cros, and A. Fert, *Interfacial Potential Gradient Modulates Dzyaloshinskii-Moriya Interaction in Pt/Co/Metal Multilayers*, Phys Rev Mater **6**, L071401 (2022).

[7] W. Jiang et al., *Direct Observation of the Skyrmion Hall Effect*, Nat Phys **13**, 162 (2017).

[8] L. Berges, E. Haltz, S. Panigrahy, S. Mallick, R. Weil, S. Rohart, A. Mougin, and J. Sampaio, *Size-Dependent Mobility of Skyrmions beyond Pinning in Ferrimagnetic GdCo Thin Films*, Phys Rev B **106**, 144408 (2022).

[9] S. K. Kim, G. S. D. Beach, K.-J. Lee, T. Ono, T. Rasing, and H. Yang, *Ferrimagnetic Spintronics*, Nat Mater **21**, 24 (2022).

[10] S. Vélez et al., *Current-Driven Dynamics and Ratchet Effect of Skyrmion Bubbles in a Ferrimagnetic Insulator*, Nat Nanotechnol **17**, 834 (2022).

[11] A. K. C. Tan, P. Ho, J. Lourembam, L. Huang, H. K. Tan, C. J. O. Reichhardt, C. Reichhardt, and A. Soumyanarayanan, *Visualizing the Strongly Reshaped Skyrmion Hall Effect in Multilayer Wire Devices*, Nat Commun **12**, 4252 (2021).

[12] R. Juge et al., *Current-Driven Skyrmion Dynamics and Drive-Dependent Skyrmion Hall Effect in an Ultrathin Film*, Phys Rev Appl **12**, 44007 (2019).

[13] K. Litzius et al., *Skyrmion Hall Effect Revealed by Direct Time-Resolved X-Ray Microscopy*, Nat Phys **13**, 170 (2017).

[14] S. Woo et al., *Current-Driven Dynamics and Inhibition of the Skyrmion Hall Effect of Ferrimagnetic Skyrmions in GdFeCo Films*, Nat Commun **9**, 959 (2018).

[15] J. Tang, Y. Wu, W. Wang, L. Kong, B. Lv, W. Wei, J. Zang, M. Tian, and H. Du, *Magnetic Skyrmion Bundles and Their Current-Driven Dynamics*, Nat Nanotechnol **16**, 1086 (2021).

[16] A. Hrabec, J. Sampaio, M. Belmeguenai, I. Gross, R. Weil, S. M. Chérif, A. Stashkevich, V. Jacques, A. Thiaville, and S. Rohart, *Current-Induced Skyrmion Generation and Dynamics in Symmetric Bilayers*, Nat Commun **8**, 15765 (2017).